The star formation rate density from $z = 1$ to 6

Michael Rowan-Robinson,[1][★] Seb Oliver,[2] Lingyu Wang,[3,4] Duncan Farrah,[5] David L. Clements,[1] Carlotta Gruppioni,[6] Lucia Marchetti,[7] Dimitra Rigopoulou[8] and Mattia Vaccari[9]

[1]*Astrophysics Group, Imperial College London, Blackett Laboratory, Prince Consort Road, London SW7 2AZ, UK*
[2]*Department of Physics and Astronomy, Astronomy Centre, University of Sussex, Brighton BN1 9QH, UK*
[3]*Department of Physics, Durham University, South Rd, Durham DH1 3LE, UK*
[4]*SRON Netherlands Institute for Space Research, Landleven 12, NL-9747 AD, Groningen, Netherlands*
[5]*Department of Physics, Virginia Tech, Blacksburg, VA 24061, USA*
[6]*INAF – Osservatorio Astronomico di Bologna, via Ranzani 1, I-40127 Bologna, Italy*
[7]*Department of Physical Science, The Open University, Milton Keynes MK7 6AA, UK*
[8]*Department of Astrophysics, University of Oxford, Keble Rd, Oxford OX1 3RH, UK*
[9]*Astrophysics Group, University of the Western Cape, Private Bag X17, 7535, Bellville, Cape Town, South Africa*

ABSTRACT

We use 3035 *Herschel*-SPIRE 500 µm sources from 20.3 deg^2 of sky in the HerMES Lockman, ES1 and *XMM*-LSS areas to estimate the star formation rate density at $z = 0$–6. 500 µm sources are associated first with 350 and 250 µm sources, and then with *Spitzer* 24 µm sources from the SWIRE photometric redshift catalogue. The infrared and submillimetre data are fitted with a set of radiative-transfer templates corresponding to cirrus (quiescent) and starburst galaxies. Lensing candidates are removed via a set of colour–colour and colour–redshift constraints. Star formation rates are found to extend from <1 to 20 000 M$_\odot$ yr^{-1}. Such high values were also seen in the all-sky *IRAS* Faint Source Survey. Star formation rate functions are derived in a series of redshift bins from 0 to 6, combined with earlier far-infrared estimates, where available, and fitted with a Saunders et al (1990) functional form. The star formation rate density as a function of redshift is derived and compared with other estimates. There is reasonable agreement with both infrared and ultraviolet estimates for $z < 3$, but we find higher star formation rate densities than ultraviolet estimates at $z = 3$–6. Given the considerable uncertainties in the submillimetre estimates, we cannot rule out the possibility that the ultraviolet estimates are correct. But the possibility that the ultraviolet estimates have seriously underestimated the contribution of dust-shrouded star formation can also not be excluded.

Key words: stars: formation – galaxies: evolution – galaxies: starburst – cosmology: observations – infrared: galaxies.

1 INTRODUCTION

The history of the determination of the evolution of the integrated star formation rate density (SFRD) has been controversial. Lilly et al. (1996) and Madau et al. (1996) gave estimates based purely on the ultraviolet (UV) light from galaxies, with a correction for extinction based on a screen model. Rowan-Robinson et al. (1997) showed from Infrared Space Observatory data that these estimates were likely to be significantly underestimated. More recent UV surveys (e.g. Schiminovich et al. 2005; Wyder et al. 2005; Dahlen et al. 2007; Reddy & Steidel 2009; Cucciati et al. 2012) and infrared (IR) surveys (e.g. Sanders et al. 2003; Takeuchi, Yoshikawa & Ishii

2003; Magnelli et al. 2011, 2013; Gruppioni et al. 2013) are now in reasonable agreement for $z < 3$. The Gruppioni et al. (2013) study of *Herschel* sources at 70, 100 and 160 µm is especially significant in capturing the total far-infrared (FIR) luminosity, and hence a more accurate estimate of the star formation rate (SFR). Madau & Dickinson (2014) have given a comprehensive review of the current situation.

At higher redshifts ($z \sim 4$–10), we have only UV estimates (Bouwens et al. 2012b, Bouwens et al.2012a; Schenker et al. 2013) and so the problem remains: is the contribution of dust-shrouded star formation being properly accounted for? The problem can be seen clearly by imagining external observations of our own Galaxy. The blue and UV light would be dominated by young stars which would be subject to an average extinction of a few tenths of a magnitude, due to the dust spread through the interstellar medium. The IR

★ E-mail: mrr@imperial.ac.uk

Table 1. Numbers of 500 μm sources in HerMES fields.

Field	Area in common with SWIRE (deg^2)	No. of 500 μm sources	Candidate lenses	No. of 500 μm sources not associated with SWIRE	Limiting 500 μm flux-density (mJy)
Lockman	7.5	957	109	368	25
ES1	3.8	478	48	205	25
XMM-LSS	9	767	72	259	30
EN1	3.1	116	23	5	40
CDFS	2.9	129	17	22	40

emission from this optically thin dust makes up the IR 'cirrus'. However, the contribution of newly formed stars embedded in dense molecular clouds would not be accounted for. In the case of our Galaxy, this would result in an underestimate of the total SFR by only about 10 per cent, but for luminous starbursts, the underestimate could be over a factor of 100.

To address this question, we really need to analyse the star formation history separately for relatively quiescent galaxies like our own and for starburst galaxies. In the latter, star formation appears to be driven primarily by major mergers, whereas for quiescent galaxies, the driver is either interaction with companions or infall of gas from the cosmic web (Daddi et al. 2010; Rodighiero et al. 2011).

The *Herschel* mission (Pilbratt et al. 2010) gives us for the first time samples of galaxies for which we have the full UV to submillimetre spectral energy distributions (SEDs) reaching out to $z = 6$ and so allows us to explore the evolution of the SFRD beyond $z = 3$. The samples we focus on in this paper are from the HerMES survey (Oliver et al. 2012), made with the SPIRE sub-millimetre camera (Griffin et al. 2010) and are selected at 500 μm, where the negative *K*-correction gives us greater visibility of the high-redshift universe than selection at 250 or 350 μm (Franceschini et al. 1991). 500 μm selection also has the benefit that in the majority of cases, we have 250 and 350 μm data, which give us valuable SED information. Rowan-Robinson et al. (2014) have given a very detailed discussion of the SEDs of a sample of 957 galaxies in the HerMES-Lockman area following on from earlier work by Rowan-Robinson et al. (2010). Here we extend the sample to the ES1 and *XMM*-LSS areas of the HerMES survey.

The structure of this paper is as follows: in Section 2, we define our samples and describe the determination of the SFR via modelling of the SEDs. In Section 3, we derive the SFR function in redshift bins from $z = 0$ to 6. In Section 4, we use this information to determine the evolution of the SFRD. Section 5 gives our discussion and conclusions.

A cosmological model with $\Lambda = 0.7$, $h_0 = 0.72$ has been used throughout.

2 DETERMINATION OF SFR THROUGH SED MODELLING

The Lockman sample has been studied in detail by Rowan-Robinson et al. (2014). Our starting point was the HerMES SPIRE (SCAT) 500 μm catalogue (Wang et al. 2014b) with sources detected at 500 μm without using any prior information from other SPIRE bands (i.e. blind 500 μm catalogue). 500 μm sources from the HerMES survey in Lockman were associated first with 350 μm sources, and only accepted as credible if there was a good (5σ) 350 μm detection, and then with 250 μm sources and with galaxies from the SWIRE photometric redshift catalogue (Rowan-Robinson et al. 2013), using automated SED fits to the SWIRE data to select the most likely 24 μm association. There are then 957 sources

for which we have SEDs from 0.36 to 500 μm, and a further 368 500–350–250 μm sources with no SWIRE counterpart. The 957 sources with SWIRE counterparts were modelled with an automatic IR template-fitting routine using a set of standard templates: M82 and A220 starbursts, a young starburst template, normal and cool cirrus templates, and an active galactic nuclei (AGN) dust torus template. These templates have been derived from full radiative-transfer treatments (Rowan-Robinson 1995; Efstathiou, Rowan-Robinson & Siebenmorgen 2000; Efstathiou & Rowan-Robinson 2003). Full details of the templates used are given via a readme page.[1]

109 lensing candidates were identified through their anomalous SEDs, which in Rowan-Robinson et al. (2014) we characterized by a set of colour–colour and colour–redshift constraints. These lensing candidates have been removed from this study, leaving a sample of 848 submillimetre galaxies with SWIRE counterparts.

We have applied a similar analysis to the ES1, EN1, *XMM*-LSS and CDFS areas within the HerMES survey. A detailed discussion of the HerMES catalogues, and their completeness and reliability is given by Wang et al. (2014b). Full details of the SWIRE photometric redshift catalogue in these areas are given via a readme page,[2] including details of reprocessing of the *XMM*-LSS and ES1 areas to take advantage of new photometry. Table 1 summarizes the areas and numbers of sources for each region. Plots of S24 versus S500 for each region (not shown here) allow an estimate of the 500 μm completeness limit for each region. Because we require sources to be detected at both 500 and 350 μm at five times the total noise (confusion plus instrumental), our completeness limits are higher than the confusion limits quoted by Nguyen et al. (2010) and Wang et al. (2014b). Only ES1 and *XMM*-LSS are of comparable depth to Lockman (∼25 mJy): these regions have been added to the present study, yielding a total area covered of 20.3 deg^2. The EN1 and CDFS areas do not play a part in the remainder of the paper.

Because our detection threshold at 500 μm is set at 5σ, where σ is the total (confusion plus instrumental) noise, we do not believe our sample is seriously compromised by completeness or confusion issues. An extensive discussion of confusion and mis-association issues was given by Rowan-Robinson et al. (2014). The chance of mis-association with the wrong 24 μm counterpart was estimated as 5 per cent.

As the templates used are derived from full radiative transfer models, they allow the SFR to be estimated for each galaxy. The conversion factors from the IR luminosity have been given by Rowan-Robinson et al. (2008). The models are spherically symmetric and do not account, for example, for the possibility of multiple starburst locations in a galaxy. In the case of cirrus components, where optically thin dust is heated by starlight, we have made a correction here for the contribution of old stars to the heating. To do this, we use the approximation noted by Rowan-Robinson (2003), so that

---

[1] http://astro.ic.ac.uk/public/mrr/swirephotzcat/templates/readme
[2] http://astro.ic.ac.uk/public/mrr/swirephotzcat/readmeSWIRErev

Table 2. Fraction of infrared (1–1000 μm) emission contributed by young stars.

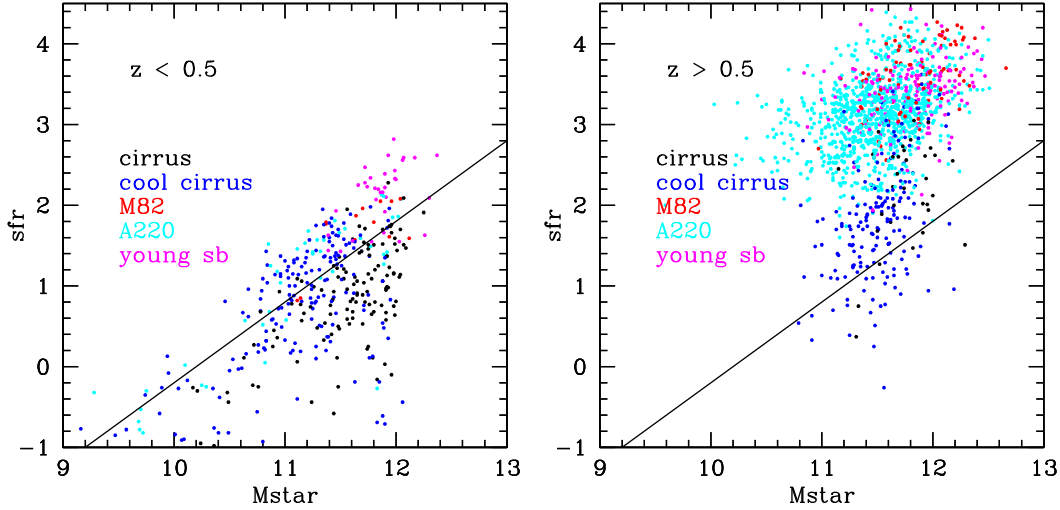| j2	1	2	3	4	5	6	7	8	9	10	11
Type	E	E'	Sab		Sbc		Scd		Sdm		sb
y	0.0	0.0	0.360	0.288	0.216	0.412	0.607	0.752	0.896	0.866	0.835

Figure 1. Star formation rate versus stellar mass for 1983 unlensed Lockman+*XMM*+ES1-SWIRE sources, colour-coded by the dominant SED template component, for $z < 0.5$ (L) and $z > 0.5$ (R). There is a reasonably clear distinction between quiescent galaxies, modelled with cirrus templates and with star formation rate <100 M$_\odot$ yr^{-1}, and starburst galaxies, with star formation rates greater than this. An indicative line of slope 1 is plotted through the $z < 0.5$ points.

the optical–near-infrared (NIR) SEDs of *Hubble* sequence galaxies can be modelled as a superposition of an elliptical galaxy template, representing stars older than 1 Gyr, and a residual component due to young stars which varies with *Hubble* type. We use the flux at 1.25 μm as a measure of the old star component.

The fraction of IR radiation contributed by young stars in a galaxy of type t, $y(t)$, is then estimated as

$$y(t) = 1 - \frac{QL(E))}{QL(t)}, \qquad (1)$$

where

$$QL(t) = \int \frac{Q_{\nu,\text{abs}} f_\nu \, d\nu}{\nu f_\nu|_{1.25\,\mu\text{m}}}, \qquad (2)$$

and $Q_{\nu,\text{abs}}$ is the absorption efficiency of the dust grains.

The SFR for cirrus components is then calculated from yL_{cirr}. Table 2 gives the calculated values of y as a function of the optical template type.

The optical templates used for the SWIRE photometric redshift catalogue were fitted with stellar synthesis codes and so give estimates of the stellar mass (Rowan-Robinson et al. 2008). Fig. 1 shows the SFR versus stellar mass for 1983 unlensed Lockman+*XMM*+ES1-SWIRE sources, colour-coded by the dominant SED template component, divided into $z < 0.5$ (L) and $z > 0.5$ (R). There is a reasonably clear distinction in Fig. 1 between quiescent galaxies, modelled with cirrus templates and with SFR < 100 M$_\odot$ yr^{-1}, and starburst galaxies, with SFRs greater than this. However, our distinction between starburst and quiescent galaxies is based on SED type not on location in the SFR-M_* diagram, unlike the 'main-sequence' locus (Brinchman, Charlot & White 2004; Daddi et al. 2007, 2010; Elbaz et al. 2007; Noeske et al. 2007; Genzel et al. 2010; Rodighiero et al. 2014). 32 of the 848 unlensed
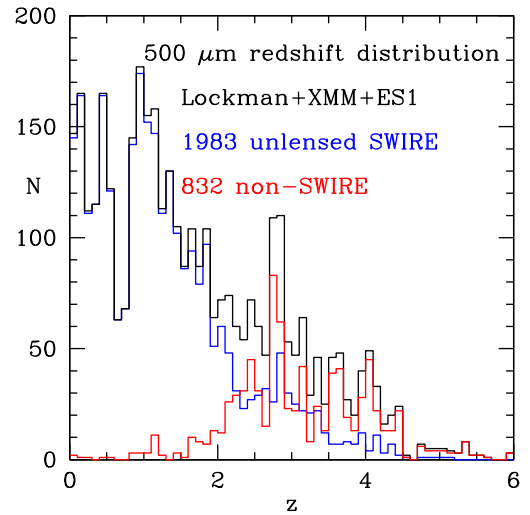

Figure 2. L: star formation rate versus redshift for HerMES Lockman+*XMM*+ES1 galaxies, with 500 μm selection limits for each template type. R: star formation rate versus redshift for 60 303 *IRAS* RIFSCz galaxies (Wang et al. 2014a). Known lenses are indicated by L and cases known to be unlensed indicated by U (Farrah et al. 2002).

Lockman galaxies are fitted with a QSO template at 0.36–4.5 μm and do not feature in Fig. 1.

Fig. 2(L) shows the SFR versus redshift for Lockman+*XMM*+ES1 sources, with loci showing the selection imposed by the 500 μm sensitivity limit of 25 mJy for different template types. Galaxies of a certain type can fall below the limit imposed by the 500 μm limit for that type because SEDs can be modelled with a
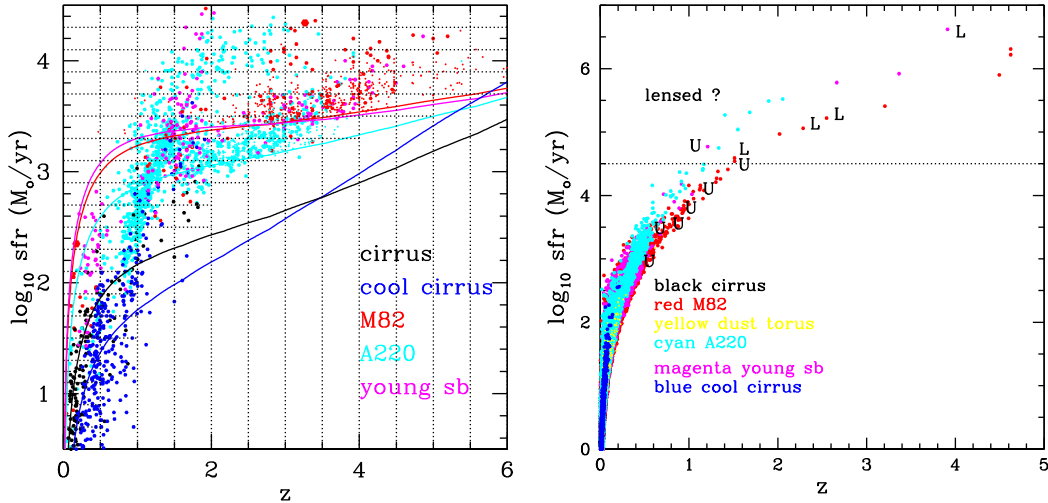
Figure 3. Redshift distribution for HerMES-Lockman+*XMM*+ES1 500 μm sample. Blue: SWIRE associated, unlensed; red: SWIRE unassociated; black: total.

mixture of template types, which contribute to different wavelength ranges. We see that the selection loci for M82 starbursts and for young starbursts are almost identical. Of the 848 unlensed Lockman galaxies, 255 use an AGN dust torus template in the FIR and submillimetre SED fit (and these do not contribute to the SFR). For only two objects is an AGN dust torus the dominant contribution to the IR luminosity.

We have also estimated photometric redshifts for the unidentified 500 μm sources from the 250–500 μm fluxes, allowing M82, Arp220 or young starburst templates, and these are shown as small filled circles in Fig. 2(L). Redshifts for these generally range from z = 2 to 6. The redshift distribution for both (unlensed) identified and unidentified sources in Lockman+*XMM*+ES1 is shown in Fig. 3. 60 per cent of our redshifts from 2 to 4 and almost all those at $z >$ 4 are unidentified sources. Cirrus galaxies at $z = 1$–2 could give similar 250–500 μm colours to starbursts at $z = 4$–6. However, it would not be possible for them to be detected at 500 and 350 μm, but not at 24 μm, 3.6 μm and in the r band. So they could not contribute to the unidentified sources. There can be no cirrus galaxies at $z > 2$ in this sample because their IR luminosity would exceed the maximum possible for an optical galaxy. Thus, it is reasonable to use only starburst templates in estimating the redshifts of unidentified sources.

It is striking that SFRs extend up to 20 000 M$_\odot$ yr^{-1}. Such enormous SFRs can presumably last for no more than 10^7 yr, compared with $\sim 10^8$ yr for local starbursts (Genzel et al. 1998; Rowan-Robinson 2000). Such high SFRs have been seen before in the *IRAS* hyperluminous galaxies (Rowan-Robinson 2000; Rowan-Robinson & Wang 2010). Fig. 2(R) shows the SFR versus redshift for the RIFSCz catalogue (Wang et al. 2014a), with known lensed sources indicated by L, and sources for which *Hubble Space Telescope* imaging (Farrah et al. 2002) shows no sign of lensing indicated by U. The boundary between lensed and unlensed sources appears to fall at a SFR of $\sim$30 000 M$_\odot$ yr^{-1}. In the case of the all-sky RIFSCz, selected at 60 μm, we see rare, exceptionally strongly lensed galaxies, in which the optical emission is also from the lensed galaxy. Typically, the surface density of such objects is 0.001 deg^{-2}. For the HerMES 500 μm-selected candidate lensed galaxies, the optical emission is from the lensing galaxy and the surface density of candidate lenses is 10 000 times greater, $\sim$10 deg^{-2}.

3 RELIABILITY OF $z > 4$ PHOTOMETRIC REDSHIFTS

The reliability of SWIRE photometric redshifts has been discussed by Rowan-Robinson et al. (2013). Provided at least five photometric bands are available, photometric redshifts have an rms accuracy better than 5 per cent and a catastrophic outlier rate <7 per cent out to $z = 1.5$. Beyond this redshift, we have few spectroscopic redshifts available and the plausibility of redshifts can only be tested through SED plotting. The 24 and 250–500 μm fluxes can be helpful here. Figs 4 and 5 show SEDs of Lockman, *XMM*-LSS and ES1 500 μm sources with photometric redshifts > 4. Most of these look plausible. 160.027 54+58.223 80, the bottom source in Fig. 3(R), has a blackbody spectrum in the optical and is therefore a star. The submillimetre source has been transferred to the unidentified category. Of the other 26 objects, one (162.681 20+57.556 06) has been fitted with a QSO template at optical–NIR wavelengths, but several others could also be fitted with a QSO template (shown as dotted loci).

We can make an independent estimate of the redshift from the submillimeter (250–500 μm data), z_{subm}, using the best-fitting M82, Arp220 or young starburst templates. This is valuable in selecting between z_{phot} aliases. For all galaxies with $z_{phot} > 2$, we have estimated z_{subm}. Fig. 6(L) shows z_{subm} versus z_{phot} for Lockman, *XMM*-LSS and S1 galaxies. We estimate the uncertainty in z_{subm} as ±30 per cent of (1+z) (see discussion of χ^2 distributions below). We have also summed χ^2_{phot} and χ^2_{subm} and estimated z_{comb}, where the combined χ^2 is a minimum. Fig. 6(R) shows a plot of z_{comb} versus z_{phot}. Generally $z_{comb} \sim z_{phot}$, with an rms uncertainty of ±10 per cent in (1+z), showing that the submillimetre data are consistent with z_{phot}. However, there are 27 catastrophic outliers (out of 388 galaxies) where (1+z_{comb}) differs from (1+z_{phot}) by more than 30 per cent from (1+z_{phot}). 12 of these outliers had $z_{phot} > 4$. For these 27 outliers, we have adopted z_{comb} rather than z_{phot} in the subsequent analysis. For $z < 2$, it is not possible to make a meaningful estimate of z_{subm} because of the presence of cirrus components, which alias catastrophically with Arp 220 starbursts.

Fig. 7 shows χ^2_{phot}, χ^2_{subm} and the sum of these for the $z_{phot} > 4$ galaxies in Lockman. The χ^2_{subm} distributions demonstrate that the
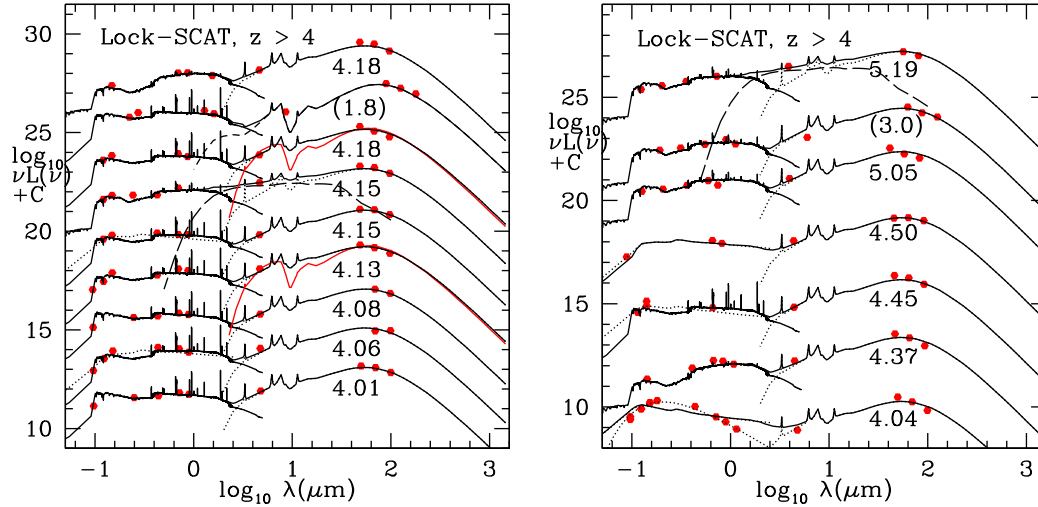
Figure 4. SEDs of Lockman-SPIRE 500 μm sources with photometric redshifts >4, labelled with the redshift. Lower redshift aliases (z_{comb}) are shown with redshift bracketed, above SED for the higher redshift alias. Dotted loci: M82 starburst, dashed loci: Arp 220 starburst, long-dashed loci: AGN dust torus, red loci: young starburst template.
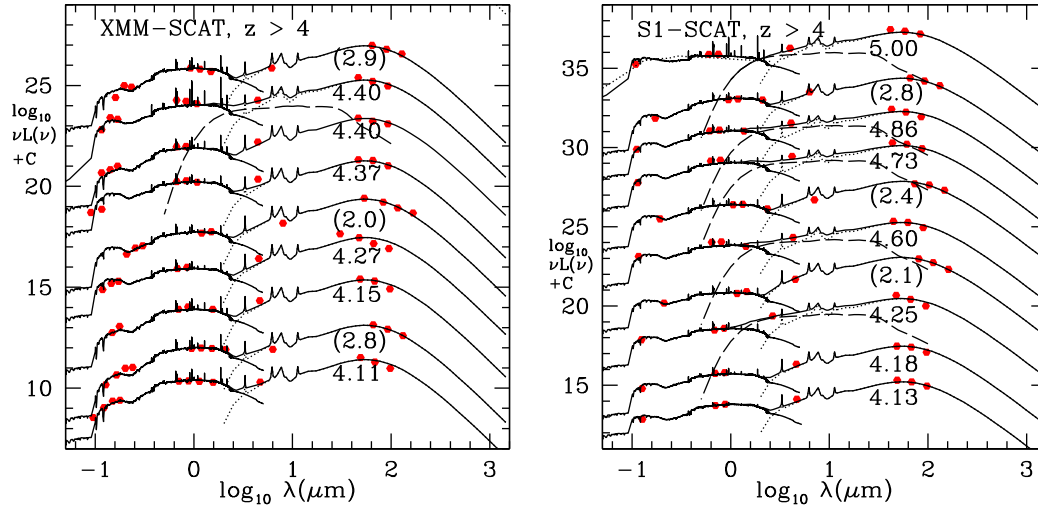

Figure 5. SEDs of SPIRE 500 μm sources with photometric redshifts > 4 in *XMM*-LSS (L) and ES1 (R). Notation as for Fig. 4.
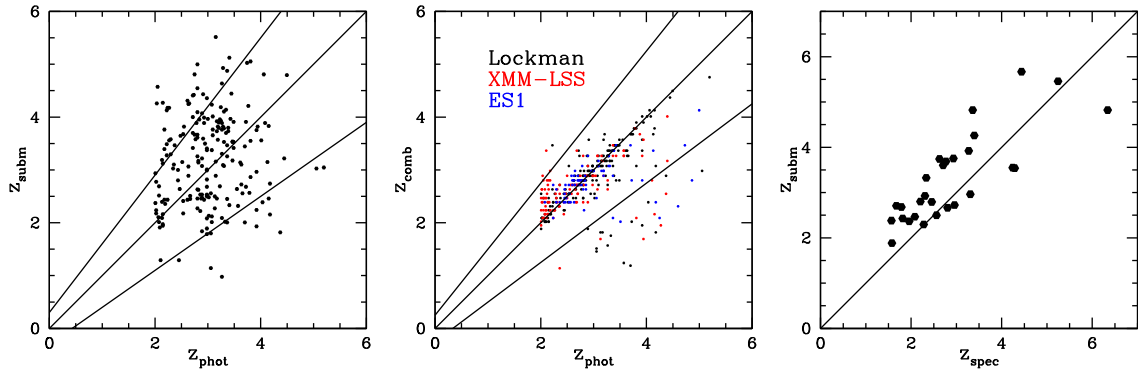

Figure 6. L: z_{subm} versus z_{phot} for Lockman, *XMM* and ES1 galaxies with $z_{phot} > 2$. The sloping loci correspond to ±30 per cent of $(1+z_{phot})$. C: z_{comb} versus z_{phot} for Lockman, XMM and ES1 galaxies with $z_{phot} > 2$. Outliers have been assigned redshift z_{comb}. R: z_{subm} versus z_{spec} for *Herschel* galaxies with spectroscopic redshifts. Spectroscopic data from Cox et al. (2011); Lupu et al. (2012); Combes et al. (2012); Riechers et al. (2013); Wardlow et al. (2013); Dowell et al. (2014) and Rowan-Robinson et al. (2013).
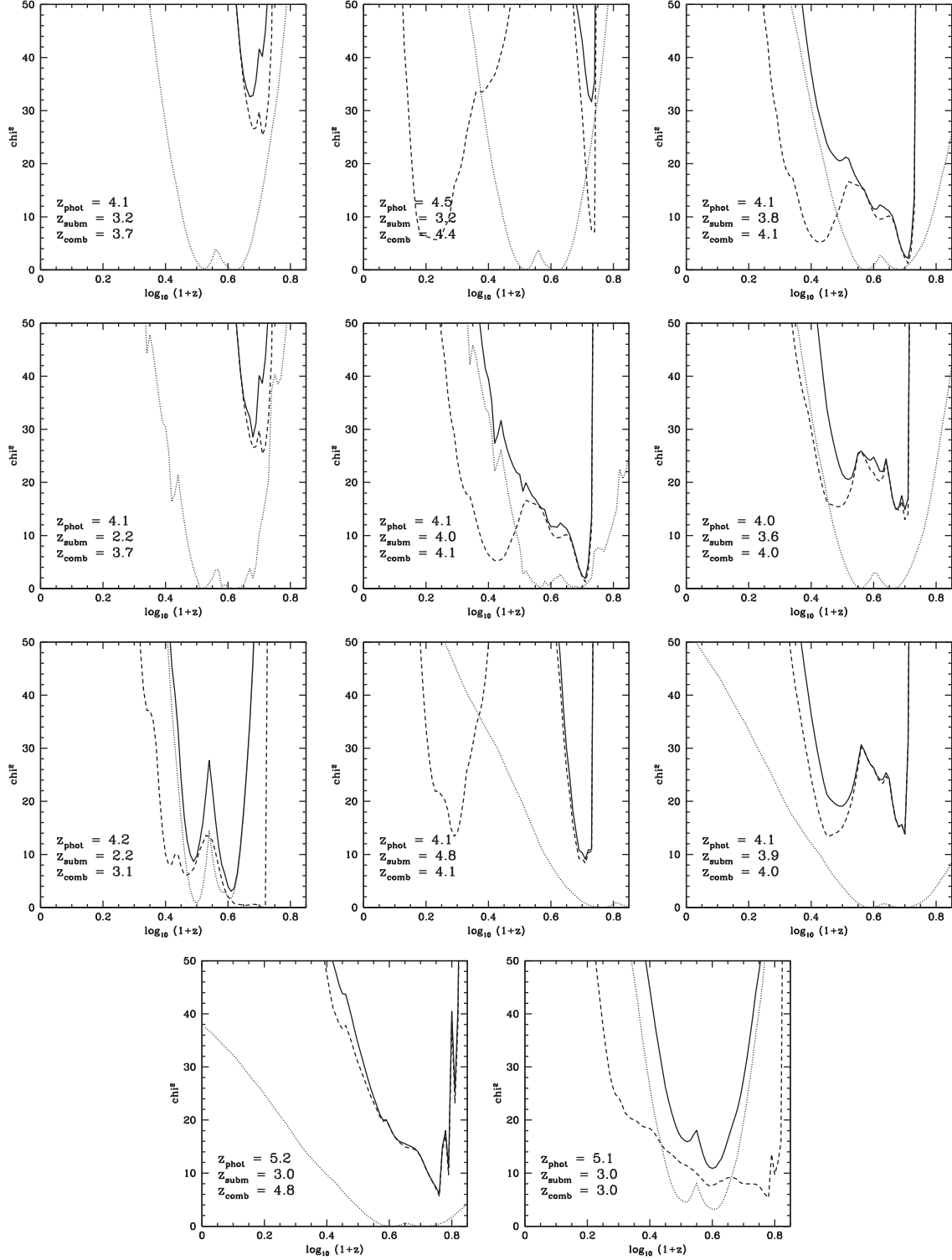
Figure 7. χ^2 distributions for Lockman-SPIRE galaxies with $z_{phot} > 4$. Broken curves: photometric redshift, dotted curves: submillimetre (250–500 µm) redshift, solid curves: combined χ^2.

uncertainty in z_{subm} is $\sim\pm 30$ per cent of $(1+z)$, due to the different redshifts generated by the different templates seen in luminous starbursts. For galaxies where z_{comb} differs significantly from z_{phot}, we have shown SED fits for both z_{phot} and z_{comb} (labelled with redshifts in brackets) in Figs 4 and 5.

We have tested the reliability of our z_{subm} estimates by applying them to 28 *Herschel* sources with measured spectroscopic redshifts (Cox et al. 2011; Combes et al. 2012; Lupu et al. 2012; Riechers et al. 2013; Rowan-Robinson et al. 2013; Wardlow et al. 2013; Dowell et al. 2014). Fig. 6(R) shows z_{subm} versus z_{spec} for these

Table 3. Galaxies with photometric redshifts >4.

RA	Dec.	i	S24 (μJy)	S250 (mJy)	S350 (mJy)	S500 (mJy)	z_{phot}	Type	χ^2	n_{bands} (opt–NIR)	z_{subm}	z_{comb}	
Lockman													
162.846 16	58.005 14	($g = 24.41$)	179.3	34.4	40.1	32.4	4.01	sb	13.0	5	3.6	4.0	
162.460 65	58.117 01	21.96	252.5	–	28.4	41.4	4.06	sb (QSO?)	7.9	6	4.8	4.1	
163.909 18	57.940 04	($g = 24.48$)	135.0	–	36.7	31.9	4.08	sb	12.6	5	3.9	4.0	
161.982 71	58.074 77	22.10	264.4	44.2	45.3	33.6	4.13	sb	25.4	6	3.2	3.7	
163.519 13	58.285 40	22.35	138.4	28.1	37.2	30.3	4.15	sb (QSO?)	1.0	5	3.8	4.1	
164.283 66	58.435 24	22.30	596.0	43.5	51.0	37.4	4.15	Scd	60.0	5	2.5	3.8	
164.026 47	57.071 53	22.28	252.3	43.2	35.2	26.0	4.18	sb	2.5	4	2.7	1.8	low-z alias
164.520 54	58.307 82	23.40	306.9	81.9	92.1	58.2	4.18	Sab	0.03	3	2.2	3.1	
160.027 54	58.223 80	18.74	168.2	69.5	57.5	31.4	4.04	QSO	61.6	11	2.4		star
161.898 94	58.164 01	23.60	315.0	66.4	59.7	35.3	4.37	Sab	22.7	4	1.8	2.9	
162.422 90	57.187 50	22.25	121.0	43.5	46.1	32.6	4.45	sb (QSO?)	5.6	4	3.2	4.4	
162.681 20	57.556 06	($g = 24.35$)	194.9	25.5	37.0	38.3	4.50	QSO	1.3	3	4.8	4.5	
161.588 35	59.658 26	23.71	156.0	48.1	35.1	31.8	5.05	Scd	4.7	5	3.0	3.0	
161.630 13	59.176 88	23.94	391.4	–	29.6	27.0	5.19	Scd	4.8	4	3.0	4.8	
ES1													
7.982 09	−43.29812	$R = 24.87$	275.8	45.6	49.7	38.8	4.13	Sab	0.02	3	2.5	3.4	
9.284 33	−44.23750	$R = 25.06$	437.0	62.5	72.5	51.5	4.18	Scd	0.03	3	3.4	3.5	
9.085 71	−42.59628	$R = 24.89$	271.8	95.7	76.3	41.3	4.25	Scd	0.85	3	2.3	2.1	low-z alias
9.111 42	−42.84052	$R = 24.44$	354.5	37.6	45.0	30.1	4.60	Scd	0.03	3	2.1	2.4	low-z alias
8.701 99	−44.48560	$R = 25.38$	423.0	31.2	36.1	27.1	4.73	Scd	0.01	3	3.5	3.9	
9.304 74	−43.03506	$R = 25.19$	504.5	39.6	36.3	26.3	4.86	Scd	0.09	3	2.9	2.8	
9.196 81	−44.42382	$R = 24.35$	249.1	39.2	43.2	41.0	5.00	sb (QSO?)	0.04	3	4.0	4.1	
XMM-LSS													
35.733 69	−5.623 05	23.42	422.0	73.1	60.9	42.1	4.11	Sbc	4.1	6	2.6	2.8	
34.260 31	−4.955 56	24.95	451.0	55.2	61.6	35.6	4.15	Sbc	3.9	4	2.0	2.2	low-z alias
36.252 77	−5.595 34	23.94	511.7	57.9	42.0	33.6	4.27	Scd	1.2	5	2.7	2.0	low-z alias
35.736 05	−4.889 50	($g = 25.02$)	421.5	40.6	51.9	40.5	4.37	Scd	11.4	6	3.7	2.6	
36.658 71	−4.146 28	24.91	288.8	46.1	45.7	48.1	4.40	Sbc	2.1	6	4.0	4.4	
34.534 69	−5.007 69	23.47	342.8	47.3	42.4	35.8	4.40	sb	4.0	5	2.3	2.9	

galaxies. The rms error in $(1 + z_{subm})/(1 + z_{spec})$ was found to be 21 per cent.

Table 3 lists all the objects with photometric redshift >4, together with z_{subm} and z_{comb}. In the end, the reliability of these redshifts can only be demonstrated with optical or submillimetre spectroscopy. This limitation, that redshifts >4 are entirely photometric, applies equally to the UV-based studies of Bouwens et al. (2012a,b) and Schenker et al. (2013).

4 THE SFR FUNCTION

We can use the data displayed in Fig. 2(L) (and the corresponding data in *XMM*-LSS and ES1) to determine the SFR function over the redshift range 0–6. We use bins of 0.5 in z, and 0.2 dex in SFR = $\log_{10}(\text{sfr})$. Ideally, we would do this for each template type but our sample is not large enough to do this, so we perform this analysis for the two broad population types, starburst (M82+A220+young starburst) and quiescent (normal cirrus + cool dust + cold dust). For each of these two populations, we use the most conservative sensitivity limit locus, the M82 template for starbursts and the normal cirrus template for quiescent galaxies.

For each bin of redshift and SFR, we estimate the contribution to the dust-enshrouded SFRD as $n/(A\,V)$, where n is the number of sources in the bin, A is the area of the survey (20.3 deg^2), and V is the comoving volume sampled by the bin. For each redshift bin, we then fit the SFR function with a Saunders functional form (Saunders

et al. 1990):

$$\psi(\text{sfr}) = \psi_0 \cdot 10^{(1-\alpha)(\text{SFR}-\text{SFR}_0)}$$
$$\times \exp\left[-(1 + 10^{(\text{SFR}-\text{SFR}_0)})^2/(2\sigma^2)\right].$$

However, because we see only the high-luminosity end of the SFR function, we cannot determine all the parameters of the luminosity function freely from the present samples on their own in all redshift bins.

For $z < 0.5$ (Fig. 8), we combine our data with the Saunders et al. (1990) 'cool' and 'warm' 60 μm luminosity functions as representative of the quiescent and starburst populations, respectively, with a conversion from 60 μm luminosity to star formation rate of SFR = $10^{-9.48}L_{60}\text{M}_\odot$ yr^{-1}, where L_{60} is in solar units (Rowan-Robinson et al. 1997). The accuracy of the Saunders et al. (1990) luminosity functions has been confirmed in many subsequent analyses, including the Wang & Rowan-Robinson (2010) determination of the 60 μm luminosity function from the *IRAS* FSS Redshift Catalogue, which gave almost identical results to Saunders et al. (1990). Other recent determinations of the FIR and submillimetre local luminosity functions include Vaccari et al. (2010), Patel et al. (2013) and Marchetti et al. (2016). There is reasonable consistency between our 500 μm selected determination of the SFR function for starburst and quiescent galaxies and those determined by conversion from the Saunders et al. (1990) warm and cool 60 μm luminosity functions, although our estimates appear high for the highest luminosity bins. For starburst/warm galaxies, we find $\alpha = 1.2 \pm 0.1$, and $\sigma = 0.60 \pm 0.03$. For quiescent/cool galaxies, we find $\alpha = 1.2$
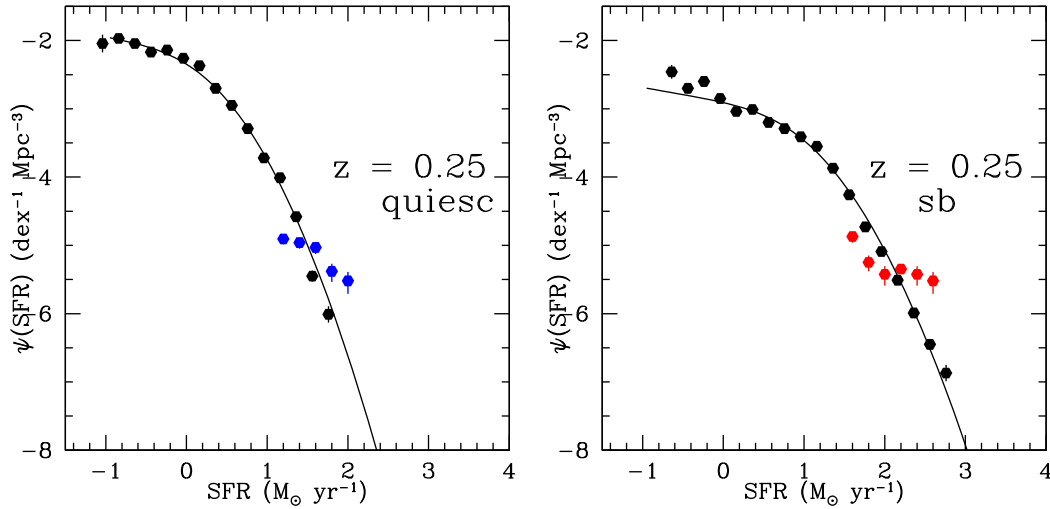
Figure 8. Star formation rate functions for $z = 0$–0.5. L: quiescent galaxies (our data in blue), R: starburst galaxies (our data in red). Black points are adapted from Saunders et al. (1990) for 'cool' galaxies (L) and 'warm' galaxies (R).

Table 4. Star formation rate function parameters.

$z =$	0.25	0.75	1.25	1.75	2.25	2.75	3.25	3.75	4.25	4.75	5.25	5.75
Quiescent												
No. of gals in fit	106	38	41									
$\log_{10}(\psi_0)$	-2.43	$[-2.51]$	$[-2.92]$									
$\log_{10}(SFR_0)$	-0.38	-0.03	0.67									
Starburst												
No. of gals used in LFs	68	95	295	219	230	252	172	158	89	14	21	5
of which, unassociated	4	6	18	23	130	158	81	132	79	12	20	5
$\log_{10}(\psi_0)$	-3.30	-3.11	-3.42	-3.50	-3.49	-3.50	$[-3.48]$	$[-3.48]$	$[-3.48]$	$[-3.48]$	$[-3.48]$	$[-3.48]$
$\log_{10}(SFR_0)$	0.27	0.93	1.57	1.66	1.66	1.80	1.68	1.85	1.88	1.69	1.76	1.65
Median no. of photom. bands	10	8	6	6	6	5	5	5	4	4	4	3
$\log_{10}$ SFRD	-1.90	-1.28	-0.95	-1.06	-1.05	-0.82	-0.99	-0.82	-0.79	-0.99	-0.92	-1.03
	±0.08	±0.21	±0.11	±0.13	$+0.27$	$+0.18$	$+0.14$	$+0.18$	$+0.14$	$+0.29$	$+0.28$	$+0.32$
					-0.09	-0.09	-0.41	-0.36	-0.41	-0.46	-0.44	-0.38

± 0.1, and $\sigma = 0.55 \pm0.05$. For all other redshift bins, we then fix $\alpha = 1.2$ but allow a range ±0.1 in estimating the uncertainty in the SFRD (which is the integral of the SFR function).

For $z = 0.5$–3.5, we combine our data with the Gruppioni et al. (2013) total IR luminosity function, using a conversion SFR = $10^{-9.70}L_{ir}M_\odot$ yr^{-1} (Rowan-Robinson et al. 1997), where L_{ir} is in solar units. For some of our redshift bins, we had to combine two of Gruppioni et al.'s bins to get the equivalent redshift range. We show their $z = 3$–4.2 function compared to our 3–3.5 function, since most of their redshifts fall in that bin. There is reasonable consistency between these independent estimates of the SFR function in the range of SFRs in common.

For quiescent galaxies at $z = 0.5$–1.5, we used $\sigma = 0.55$ but allowed a range of ± 0.05 in estimating the uncertainty in the SFRD. We also fixed ψ_0 at the values determined by Gruppioni et al. (2013).

For starburst galaxies in the range $z = 0$–3, we find a best fit of $\sigma = 0.60$. We allow a range in σ of ±0.03 in estimating the uncertainties of other parameters. ψ_0 and SFR_0 were allowed to be free parameters.

For $z > 3.5$, we have only the estimates of the SFR function at very high values of the SFR from our samples and so fix $\alpha = 1.2$, $\sigma = 0.60$. We also note that for $z = 0$–3, the parameter ψ_0 is consistent with being constant, with an average value $10^{-3.48}$dex^{-1}Mpc^{-3}, so for $z > 3$, we fix ψ_0 at this value. However, in estimating the uncertainty in the integrated SFRD in each redshift bin, we allow both ψ_0 and SFR_0 to vary by ±0.5 dex (this is illustrated in Fig. 10). Because we have data only at high luminosities and SFRs at these redshifts, we have to apply some constraint to the SFR function parameters, particularly ψ_0, to avoid abrupt changes in this function. We have also shown results in Fig. 11 assuming that ψ_0 varies as $(1 + z)^{-1}$, as assumed by Gruppioni et al. (2013), open circles in Fig. 11. These give slightly lower values of the SFRD. The issue that we are probing only the high-luminosity end of the SFR function at $z > 3$ is common to other studies, e.g. Cucciati et al. (2012) and Gruppioni et al. (2013).

Table 4 summarizes the parameters for the SFR function in each redshift bin, with square brackets denoting prior fixed values. Figs 8 and 9 show a montage of these SFR functions, with the fitted Saunders forms. There is a tendency for the very highest SFR bins to
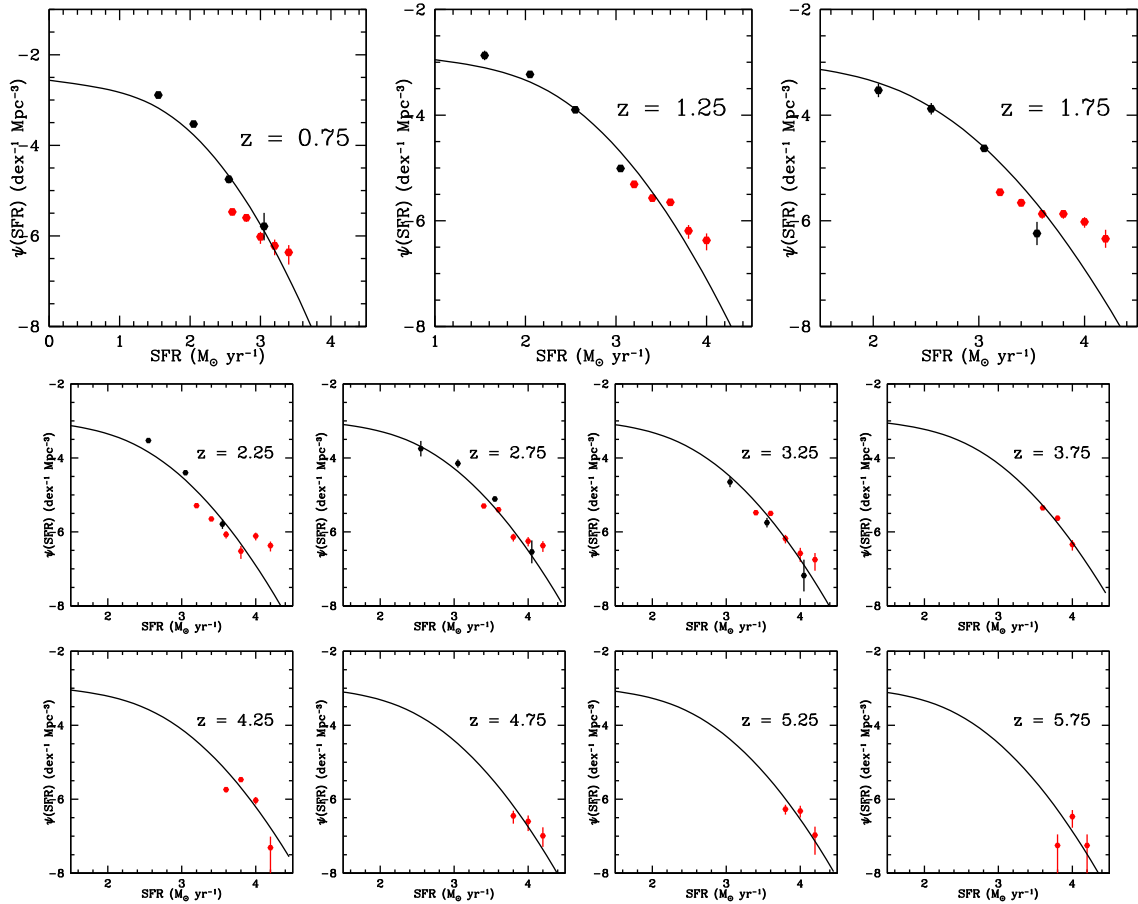
Figure 9. Star formation rate functions for starburst galaxies for $z = 0.5$–6.0, in bins of 0.5 in redshift. Red points are from present HerMES-SWIRE study, black points are from Gruppioni et al. 2013.

be higher than the fitted curves for $z < 3.5$ but these are generally based on quite small numbers of sources.

Fig. 10(L) shows the evolution of SFR_0 and ψ_0 with redshift and fits to these with the functional form introduced by Rowan-Robinson (2009) in modelling IR and submillimetre source-counts:

$$\psi_0(t) = a_0 + (1 - a_0)\exp[Q(1 - t/t_0)]((t/t_0)^P - (t/t(z_f))^P).$$

As a check, we show in Fig. 10(R) a fit to the 500 μm differential source-counts with these assumed evolution rates for the different components. The predicted background intensity at 500 μm is 3.3 nW m^{-2}sr^{-1}, consistent with direct measurements (2.40±0.60: Fixsen et al. 1998; 2.70 ±0.67: Lagache et al. 2000) and stacking analysis (2.80 + 0.93–0.81; Bethermin et al. 2012).

5 EVOLUTION OF THE SFRD

We are now in a position to show the evolution of the SFRD with redshift for quiescent galaxies, starbursts, and for the combined total (Fig. 11). This can be compared with the data compiled by Madau & Dickinson (2014). The uncertainties we have shown fully take into account the effect of varying the parameters of the SFR function, except that at $z > 3$, we have not allowed variation of the parameters α and σ. To indicate the uncertainties associated with the photometric redshifts, we have shown a range of redshift corresponding to the rms uncertainty for the median number of photometric bands in each redshift bin (last line of Table 4), taken from Rowan-Robinson

et al. (2013, fig. 15). Catastrophic photometric redshift outliers are a negligible problem for $z < 1$ (<1.5 per cent), and not a big problem for $z = 1$–2 (few per cent). Our analysis combining 0.36–4.5 μm photometric redshift and 250–350 μm submillimetre redshift estimates for $z > 2$ galaxies identified 27 catastrophic outliers out of 388 objects (7 per cent), and we substituted z_{comb} for z_{phot} for these outliers.

For the 500 μm sources unassociated with SWIRE objects, the redshifts, determined only from 250–500 μm data, are highly uncertain, with an estimated range of values ±30 per cent of $(1+z)$ due to the range of template types seen in the submillimetre (and a direct estimate from known spectroscopic redshifts of ±21 per cent). Extensive discussions of finding high-redshift ($z > 4$) galaxies purely from submillimetre photometry have been given by Dowell et al. (2014) and Asboth et al. (2016). The situation can be improved in the future by submillimetre spectroscopy of these sources. We believe the redshift uncertainties are unlikely to be responsible for the high SFRD we find at $z = 3$–6.

There is reasonable agreement between our results and those of Madau & Dickinson (2014), for $z < 3.5$. Working at 500 μm allows us to make a good determination of the SFRD at $z = 3.5$–4.5, and a more uncertain determination, based on small numbers of galaxies, at $z = 4.5$–6. Our SFRD is higher than that of Gruppioni et al. (2013) at $z = 3$–4.5, but the latter is based on very few galaxies and is quoted by the authors as essentially a lower limit. Our values are also higher than UV estimates at $z = 3.5$–6, by a factor of 2 to 3, with the lower value applying if we assume negative density evolution,
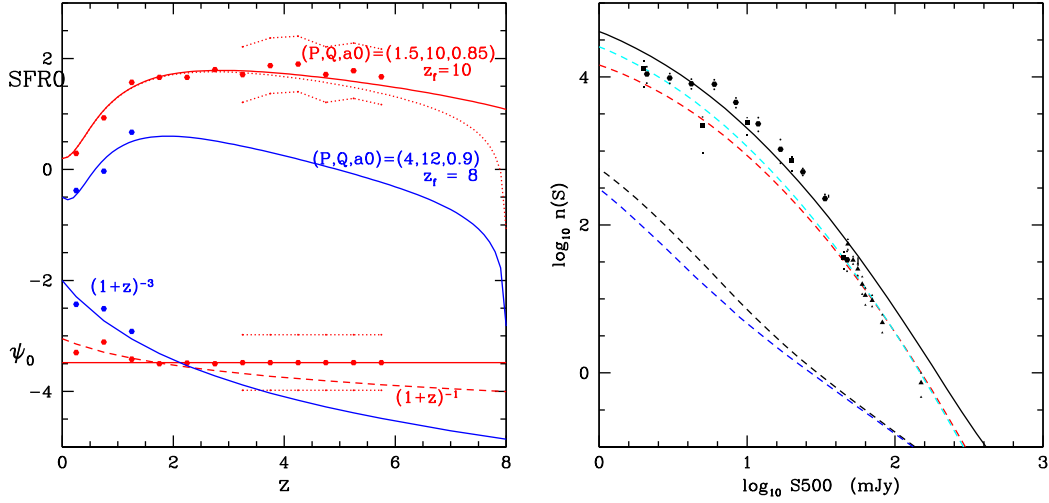
Figure 10. L: ψ_0 (lower points) and SFR_0 (upper points) as a function of redshift for quiescent galaxies (normal cirrus plus cool dust; blue) and starburst galaxies (M82 + A220 + young starburst; red) as a function of redshift, with simple analytical fits. R: differential 500 μm counts from HerMES and H-ATLAS surveys (Clements et al. 2010; Glenn et al. 2010; Oliver et al. 2010; Bethermin et al. 2012) compared with prediction of evolutionary model derived here. Black dashed locus: cirrus, blue: cool cirrus, red: M82 starburst, green: A220, black continuous locus: total.
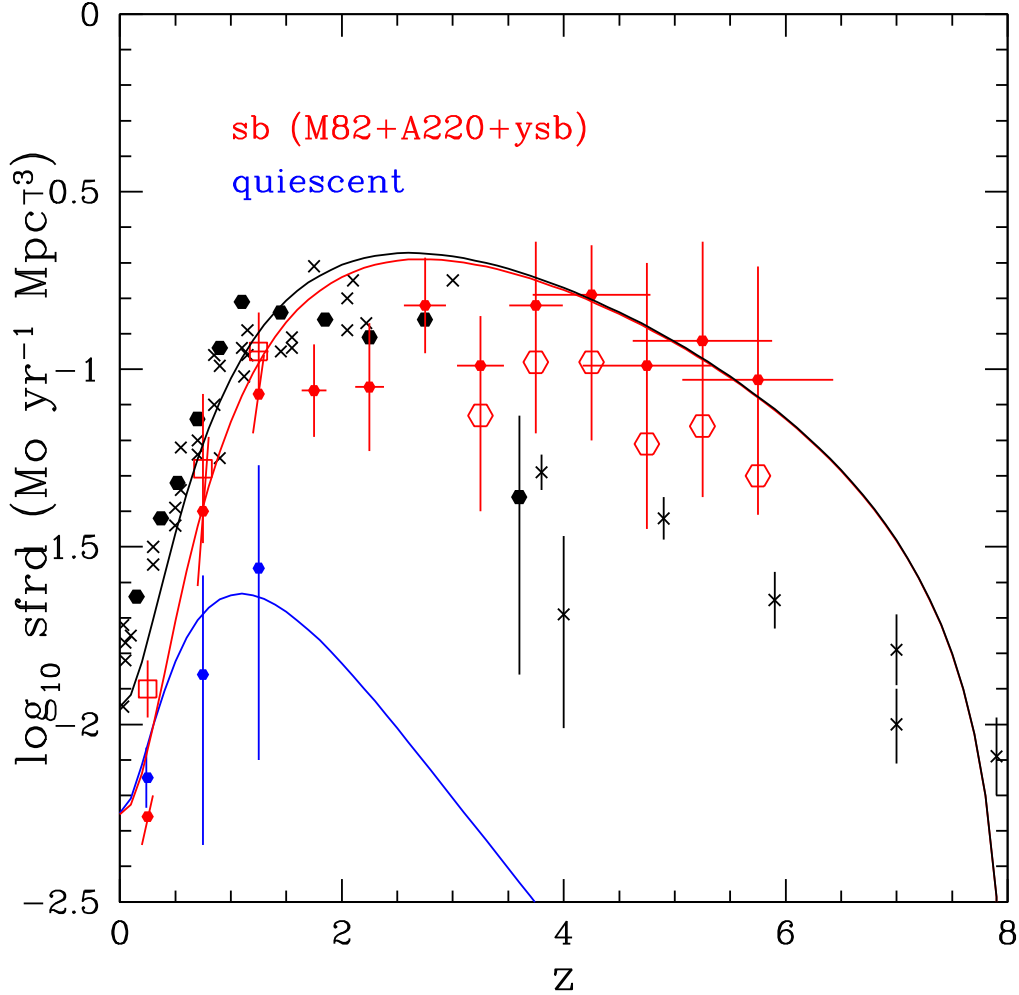
Figure 11. Star formation density as a function of redshift. Crosses: optical and ultraviolet data summarized by Madau & Dickinson (2014); black filled hexagons: FIR data of Gruppioni et al. (2013); filled red hexagons: starburst galaxies from present work derived from 500 μm sample; filled blue hexagons: quiescent galaxies from present work; open squares: sum of starburst and quiescent contributions; open circles at $z > 3$: effect of assuming ψ_0 varies as $(1 + z)^{-1}$.

with ψ_0 varying as $(1 + z)^{-1}$. Although the uncertainties in the submillimetre estimates mean that we cannot rule out the possibility that the UV estimates are correct, the higher values of the SFRD that we find could also be attributed to the fact that UV estimates are not able to assess the contribution of embedded star formation. Note that the UV estimates of Bouwens et al. (2012a,b) and Schenker et al. (2013) do not include any correction for extinction by dust, though those of Cucciati et al. (2012) do. Our high estimates of the SFRD at $z > 4$ are supported by the estimates of the SFRD derived from γ-ray bursts (Kistler et al. 2009). Mancuso et al (2016) argue that uv estimates of the SFRD at high redshift are an underestimate due to the effects of extinction.

6 DISCUSSION AND CONCLUSIONS

Our conclusion is that the epoch of high SFRD, and hence of rapid heavy element formation, stretches from redshift 4 to redshift 1. This is a significantly earlier start to the epoch of high SFRD than assumed in previous studies. This may pose problems for semi-analytic models for galaxy formation, which tend to set the epoch of intense star-formation at $z = 2$–1. Gruppioni et al. (2015) have discussed the consistency of the submillimetre luminosity function evolution with semi-analytic models. Their conclusion that the semi-analytic models underpredict the high SFR seen in starburst galaxies at $z > 2$ is strengthened by the results of this paper.

McDowell et al. (2014) have constructed a sample of $z > 4$ submillimetre galaxies by selecting HerMES sources with $S(500)>S(350)>S(250)$. While only three of our Table 3 $z > 4$ samples satisfy $S(500)>S(350)$, it is interesting that assuming the submillimetre luminosity function does not evolve from $z = 2$ to 5; they conclude that the SFRD from $z = 4$ to 6 is between 1 and 3 times the UV estimates, depending on which luminosity function they use.

Luminous star-forming galaxies at redshift 5–6 had significant dust opacities in their star-forming regions. If this dust originates in Population 2 stars, this in turn has implications for the epoch when star formation commenced, as this must be $\sim$1 Gyr before $z = 6$. Michalowski, Watson & Hjorth (2010) have emphasized the problems posed by some high-redshift submillimetre galaxies for the assumption of AGB dust formation.

Our estimates of the SFRD at $z > 4$ are based entirely on very exceptional objects, with SFRs > 3000 M$_\odot$ yr^{-1}. Presumably, the lifetime of such exceptional starbursts is significantly shorter than the $\sim 10^8$ yr seen in local starbursts, but they still need to be understood in the context of semi-analytic galaxy formation models. We believe we have efficiently removed lensing objects from our study and that these represent real SFRs. However, it is possible that some of the 500 μm sources not associated with SWIRE galaxies may be lensed and this could reduce our SFRD estimates at high redshift. If the fraction of lensed objects amongst the unassociated sources was the same as for the *Herschel* sources associated with SWIRE galaxies, i.e. 11 per cent, then the SFRD at $z > 4$ would need to be reduced by this factor. This would not alter our conclusions.

While our estimate of the SFRD is highly uncertain, especially at $z > 4.5$, it demonstrates the potential of submillimetre-selected samples of galaxies for probing the high-redshift universe and the need for further work, especially spectroscopy and submillimetre imaging, on these high-redshift submillimetre galaxies.

REFERENCES

Asboth V. et al., 2016, MNRAS, preprint (arXiv:1601.02665)
Bethermin M. et al., 2012, A&A, 542, A58
Bouwens R. J. et al., 2012a, ApJ, 752, L5
Bouwens R. J. et al., 2012b, ApJ, 754, 83
Brinchman J., Charlot S., White S. D. M., 2004, MNRAS, 351, 1151
Clements D. L. et al., 2010, A&A, 518, L8
Combes F. et al., 2012, A&A, 538, L4
Cox P. et al., 2011, ApJ, 740, 63
Cucciati O. et al., 2012, A&A, 539, 31
Daddi E. et al., 2007, ApJ, 670, 156
Daddi E. et al., 2010, ApJ, 714, L18
Dahlen T., Mobasher B., Dickinson M., Ferguson H. C., Giavalisco M., Kretchmer C., Ravindranath S., 2007, ApJ, 654, 172
Dowell C. D. et al., 2014, ApJ, 780, 75
Efstathiou A., Rowan-Robinson M., 2003, MNRAS, 343, 322
Efstathiou A., Rowan-Robinson M., Siebenmorgen R., 2000, MNRAS, 313, 734
Elbaz D. et al., 2007, A&A, 468, 33
Farrah D., Verma A., Oliver S., Rowan-Robinson M., McMahon R., 2002, MNRAS, 329, 605
Fixsen D. J., Dwek E., Mather J. C., Bennett C. L., Shafer R. A., 1998, ApJ, 508, 123
Franceschini A., Toffolatti L., Mazzei P., Danese L., de Zotti G., 1991, A&AS, 89, 285
Genzel R. et al., 1998, ApJ, 498, 579
Genzel R. et al., 2010, MNRAS, 407, 2091
Glenn S. J. et al., 2010, MNRAS, 409, 109
Griffin M. J. et al., 2010, AA, 518, L3
Gruppioni C. et al., 2013, MNRAS, 432, 23
Gruppioni C. et al., 2015, MNRAS, 451, 3419
Kistler M. D., Yuksel H., Beacom J. F., Hopkins A. M., Wyithe J. S. B., 2009, ApJ, 705, L104
Lagache C., Haffner L. M., Reynolds R. J., Tuffte S. L., 2000, A&A, 354, 247
Lilly S. J., Le Fevre O., Hammer F., Crampton D., 1996, ApJ, 460, L1
Lupu R. E. et al., 2012, ApJ, 757, 1352
Madau P., Dickinson M., 2014, ARA&A, 52, 415
Madau P., Ferguson H. C., Dickinson M. E., Giavalisco M., Steidel C. C., Fruchter A., 1996, MNRAS, 283, 1388
Magnelli B., Chary R. R., Dickinson M., Le Borgne D., Frayer D. T., Willmer C. N. A., 2011, A&A, 528, A35
Magnelli B. et al., 2013, A&A, 553, A132
Marchetti L. et al., 2016, MNRAS, 456, 1999
Marcuso C., Lupi A., Shi J., Gonzalez-Nuevo J., Aversa R., Danese L., 2016, ApJ, 823, 128
Michalowski M. J., Watson D., Hjorth J., 2010, ApJ, 712, 942
Nguyen H. T. et al., 2010, A&A, 518, L5
Noeske K. G. et al., 2007, ApJ, 660, L47

Oliver S. J. et al., 2010, A&A, 518, L21
Oliver S. J. et al., 2012, MNRAS, 424, 1614
Patel H., Clements D. L., Vaccari M., Mortlock D. J., Rowan-Robinson M., Perez-Fournon I., Afonso-Luis A., 2013, MNRAS, 428, 291
Pilbratt G. et al., 2010, A&A, 518, L1
Reddy N. A., Steidel C. C., 2009, ApJ, 692, 778
Riechers D. A. et al., 2013, Nature, 496, 329
Rodighiero G. et al., 2011, ApJ, 739, L40
Rodighiero G. et al., 2014, MNRAS, 443, 19
Rowan-Robinson M., 1995, MNRAS, 272, 737
Rowan-Robinson M., 2000, MNRAS, 316, 885
Rowan-Robinson M., 2003, MNRAS, 344, 13
Rowan-Robinson M., 2009, MNRAS, 394, 117
Rowan-Robinson M., Wang L., 2010, MNRAS, 406, 720
Rowan-Robinson M. et al., 1997, MNRAS, 289, 490
Rowan-Robinson M. et al., 2008, MNRAS, 386, 697
Rowan-Robinson M. et al., 2010, MNRAS, 409, 2
Rowan-Robinson M., Gonzalez-Solares E., Vaccari M., Marchetti L., 2013, MNRAS, 428, 1958

Rowan-Robinson M. et al., 2014, MNRAS, 445, 3848
Sanders D. B., Mazzerella J. M., Kim D. C., Surace J. A., Soifer B. T., 2003, AJ, 126, 1607
Saunders W., Rowan-Robinson M., Lawrence A., Efstathiou G., Kaiser N., Ellis R. S., Frenk C. S., 1990, MNRAS, 242, 318
Schenker M. A. et al., 2013, ApJ, 768, 196
Schiminovich D. et al., 2005, ApJ, 619, L47
Takeuchi T. T., Yoshikawa K., Ishii T. T., 2003, ApJ, 749, L38
Vaccari M. et al., 2010, A&A, 518, L20
Wang L., Rowan-Robinson M., 2010, MNRAS, 401, 35
Wang L., Rowan-Robinson M., Norberg P., Heinis S., Han J., 2014a, MNRAS, 442, 2739
Wang L. et al., 2014b, MNRAS, 444, 2870
Wardlow J. L. et al., 2013, ApJ, 762, 59
Wyder T. K. et al., 2005, ApJ, 619, L15

This paper has been typeset from a TEX/LATEX file prepared by the author.